Correlation Between Structure and Properties of Low-Carbon Cu-Ni-Mo-Ti-Nb Ultrahigh-Strength Steel

G. Mandal, S.K. Ghosh, D. Chakrabarti, and S. Chatterjee

Low-carbon Cu-Ni-Mo-Ti-Nb steel having more than 1700 MPa tensile strength and good low-temperature impact toughness was successfully designed and processed for automobile, defence and structural applications. The steel was thermomechanical controlled processed at a different finish rolling temperatures (750-850 °C) and cooled at two different conditions: air cooling and water quenching. Evolutions of microstructure and precipitates were thoroughly characterised to understand the effect of different factors, such as steel composition, finish rolling temperature and cooling rate on the mechanical properties. The results indicate that the steel processed at 750 °C finish rolling temperature (FRT) followed by water quenching has exhibited superior tensile properties with a yield strength of 1034-1449 MPa, the tensile strength of 1598-1726 MPa and total elongation of 10-13%. Such an ultrahigh-strength level is primarily attributed to the combined effect of lower bainite dominated microstructure along with precipitation hardening. The satisfactory low-temperature toughness is promoted by low finish rolling temperature and higher amount of misorientation offered by the boundaries within the lower bainite.

1. Introduction

Advanced high-strength steels (AHSS) have been extensively used for automotive and structural applications for several decades. The microstructures of the first generation of AHSS consisted of mainly ferrite, and the second generation was austenite-based. The recent interest worldwide is to develop a new class of steels as the third generation of AHSS. The third generation AHSS lies in between the first generation steels such as DP, HSLA and TRIP-assisted steel and the second generation steels such as austenitic stainless steel and TWIP steel. The steels to be designed are based on minimum alloy addition and multiphase microstructures comprising of ferrite, bainite and martensite with a significant amount of metastable austenite so that the best possible combination of strength and ductility can be achieved economically. In general, the third generation AHSS having 850-950 MPa proof strength is referred to as the advanced ultrahigh-strength steels (Ref 1). In this context, J. G. Speer et al. (Ref 2) proposed the quenching and partitioning (Q & P) treatment to satisfy the required properties by developing multiphase microstructure containing martensite and/or bainite along with sufficient amount of retained austenite. On the other hand, H. K. D. H. Bhadeshia introduced super bainite concept in a high-carbon

(0.78-0.98 wt.%) steel to reach as high a 2 GPa strength level with satisfactory fracture toughness (Ref 3). In addition, the nano-scale structure of fine carbide-free laths of bainitic ferrite with films of retained austenite achieved ultrahigh-strength level without mechanical processing or rapid cooling and expensive alloying additions (Ref 4, 5). Thus, there is an increasing demand for the development of low-carbon advanced ultrahigh-strength steel with good ductility, weldability, manufacturing flexibility and recyclability, besides economic and environmental advantages for satisfying the application requirements (Ref 6-8). However, the alloy design and optimisation of thermomechanical controlled processing (TMCP) are the two significant ways of developing AHSS with an excellent combination of mechanical properties, avoiding any expensive heat treatment (Ref 9, 10).

TMCP is a simple, cost-effective and efficient process for the production of low-carbon high-strength steels which fully communicates with the chemical composition, various processing parameters and different metallurgical aspects (Ref 11). Although the increase in the carbon content of AHSS can be an economical and simplest way of increasing the strength, it depreciates the ductility, toughness and weldability by the formation of coarse carbide (Ref 12). Considering this aspect, C content is maintained at a low level and other alloying elements such as Cu, Ni, Mn, Cr and Mo along with the microalloying elements, i.e. Nb, Ti and V are added to develop ultrahigh-strength steels without sacrificing the others properties (Ref 13). In high-strength and low-alloy (HSLA) steel with low carbon content, the multiple microalloying elements are used at different combinations like (Ti + V), (Ti + Nb) or (Ti + Nb + V) to utilise their synergistic effect for achieving the maximum level of strength by grain refinement and precipitation hardening (Ref 14, 15). It is a fact that Ti addition in Nb-bearing steel can form coarse precipitates that can be detrimental to the properties (Ref 16). However, it is also reported (Ref 16, 17) that the introduction of an optimum level of Ti can be beneficial in Nb-bearing steels as Ti combines with N to form TiN, which prevents austenite grain growth and also

G. Mandal, S.K. Ghosh, and S. Chatterjee, Department of Metallurgy and Materials Engineering, Indian Institute of Engineering Science and Technology, Shibpur, Howrah 711103, India; D. Chakrabarti, Department of Metallurgical and Materials Engineering, Indian Institute of Technology, Kharagpur 721302, India. Contact e-mail: skghosh@metal.iiests.ac.in.

increases the strengthening from fine NbC precipitates (instead of coarser Nb(C, N)). Y. Funakawa et al. (Ref 18) suggested that the Ti and Mo content should be within 0.10-0.35 wt.% and more than 0.25 wt.%, respectively, for achieving 1000 MPa tensile strength. Many times, the target strength was compensated by the addition of some amount of Nb and V which form complex precipitates together with Ti and Mo (Ref 19). The addition of Mo in low-carbon microalloyed steel can increase the thermal stability of TiC precipitates at high temperature during TMCP (Ref 20).

The high Ni content provides solid solution strengthening as well as improves ductility by lowering the austenite transformation temperature (Ref 21). It is also reported that more than 0.8 wt.% of copper addition in steel can significantly enhance the strength by ε-Cu precipitation without any loss of ductility and impact toughness (Ref 22, 23). It is reported earlier that hot-rolled Ti-Nb microalloyed steel achieved a yield strength of 770 MPa (Ref 24). Furthermore, offline quenching and tempering produced ultrahigh-strength steel plates with a yield strength of 960 MPa (Ref 25). Recently, Li et al. have developed a TMCP-processed low-carbon (0.15 wt.%) microalloyed steel with 750 MPa proof strength and 19% ductility (Ref 26). Another research group processed 0.05 wt.% C microalloyed steel to achieve similar strength level with a small increment in elongation (Ref 27). In this context, understanding the combined effect of steel composition and TMCP parameters for achieving the desired properties of low-carbon, microalloyed HSLA steel is necessary, but is still lacking (Ref 28). To the best of knowledge, development of low-carbon HSLA steel with a yield strength of $\approx$ 1400 MPa by TMCP process without any heat treatment has not been reported earlier.

Therefore, on the basis of the previous studies, the present study aims to develop a novel low-carbon Cu-Ni-Mo-Ti-Nb steel with ultrahigh yield strength along with satisfactory ductility and good low-temperature toughness. To understand the effect of TMCP parameters, the effects of various FRTs and cooling conditions on the mechanical properties are investigated. Finally, the correlation between the processing, microstructure, precipitation and mechanical properties of the proposed steel is to be established.

2. Experimental Details

A low-carbon ultrahigh-strength microalloyed steel was prepared in a laboratory scale 25 kVA air induction melting furnace. The chemical composition (wt.%) of the investigated steel is reported in Table 1. After cropping the top section of the ingot ($\approx$ 10 kg) containing shrinkage pipes, the remaining portion of 250 mm × 60 mm × 60 mm-sized ingot was hot forged down to about 15 mm × 15 mm cross section. The forged bars were soaked at 1200 °C and subsequently subjected to TMCP with three different FRTs (850, 800 and 750 °C) according to the laboratory scale schedule as schematically shown in Fig. 1 using two high rolling mill (10 HP). Finally, the rolled plates ($\approx$ 6 mm) were cooled down to ambient temperature using two different conditions (air cooling, AC, and water quenching, WQ). More than 50% deformation was applied below the non-recrystallisation temperature (T_{NR}), irrespective of FRT to sufficiently deform the austenite. The T_{NR} value was estimated by the following equations based on chemical composition (C, V and Nb all are in wt.%) and applied strain per pass (ε) (Ref 29, 30):

$$T_{NR} = 203 - 310C - 149\sqrt{V} + 657\sqrt{Nb} + 683e^{-0.36\varepsilon} \quad \text{(Eq 1)}$$

where

$$\varepsilon = \frac{2}{\sqrt{3}}\ln(h_i/h_f) \quad \text{(Eq 2)}$$

where h_i and h_f are the initial and final thickness of the rolled plate, respectively. The calculated value of T_{NR} is 945 °C as mentioned in Table 1.

After TMCP, all the specimens were prepared separately for microstructural characterisation, hardness and tensile testing. First of all, the TMCP specimens were prepared metallographically and etched with 2% nital solution for detail microstructural investigation using Carl Zeiss, Axiovert 40 Mat optical microscope (OM) as well as Hitachi scanning electron microscope (SEM) (HITACHI, S-3400 N) operated at 20 kV in secondary electron mode. The image analysis was carried out on the captured optical and SEM micrographs to quantify the microstructural parameters using Axiovision software. For transmission electron microscopy (TEM), typical 3-mm-diameter discs were punched out from thin foils and subjected to twin jet electro-polishing, using a mixture of electrolyte of 90% glacial acetic acid and 10% perchloric acid at temperature of about 12 °C. Thin electron transparent samples were subsequently examined in Tecnai, G2 model TEM at 200 kV. Microtexture of the samples was studied using electron
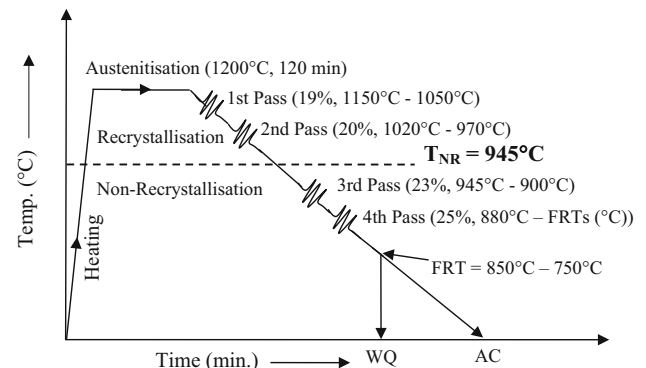
Fig. 1 Schematic diagram of thermomechanical controlled processing schedule at the laboratory scale. FRT, T_{NR}, WQ and AC stand for finish rolling temperature, non-recrystallisation temperature, water quenching and air cooling, respectively

Table 1 Chemical composition of the investigated steel (wt.%)

| C	Mn	Si	Cu	Ni	Mo	Ti	Nb	S	P	N	T_{NR}
0.16	1.96	0.31	1.62	3.27	1.38	0.05	0.07	0.01	0.01	0.0065	945 °C

backscatter diffraction (EBSD) facility attached with Zeiss EVO 60 SEM. A minimum misorientation of 2° was considered in view of the angular resolution limit of EBSD. The texture was represented in terms of inverse pole figure maps along the normal direction (ND-IPF) and orientation distribution function on $\phi_2 = 45°$ section of Euler space.

The Vickers hardness (HV) values of the samples were evaluated in a universal hardness tester (Innovatest Verzus-750CCD), using 30 kgf load for 20 s dwelling time. Average values of six measurements for each sample were reported. According to ASTM E8 M standard, flat sub-size tensile specimens (100 mm total length), having a gauge length of 25 mm, gauge width of 6.35 mm and thickness of 3 mm were prepared from the rolled plate in the longitudinal direction. The tests were carried out with the crosshead speed of 0.5 mm/min in an Instron 4204 testing machine at room temperature with an extensometer. Three specimens were tested for each variant, and the average values were reported. The Charpy V notch impact testing of the sub-size samples ($55 \times 10 \times 5$ mm^3 with 2 mm notch) following the ASTM standard (ASTM: Vol. 03.01: E23 - 96) with the flat surface along the plane of rolling was conducted at room temperature (20 °C) as well as at low temperature (-40 °C). To carry out the tests at sub-zero temperatures, samples were soaked in a bath, containing a mixture of acetone and liquid nitrogen for sufficient time of about 15 min. The average of three consistent test results was reported as the impact energy value for the corresponding test temperature of a particular sample. It is important to mention here that impact testing is widely applied in industry to determine the low-temperature impact toughness of steels, used in service. The fractographic feature of impact fracture surface was investigated by SEM.

3. Results and Discussion

3.1 Optical and Scanning Electron Microscopy

The continuous cooling transformation (CCT) study can explain the formation of different microstructural constituents at different cooling conditions. Therefore, the CCT diagram is constructed in Fig. 2 using JMatPro (Java-based Materials Properties) software. Figure 3(a, b, c, d, e and f) shows the
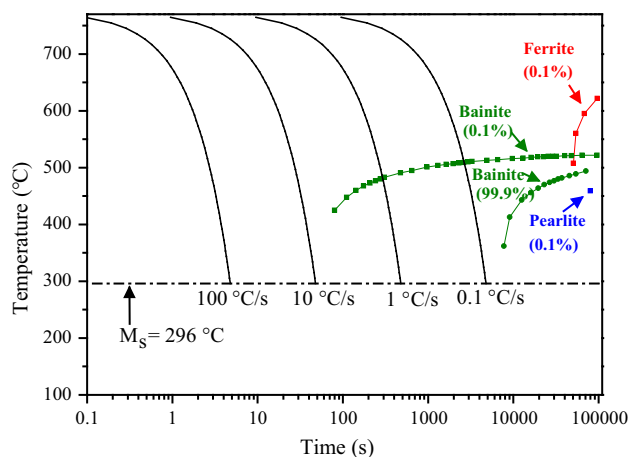
Fig. 2 CCT diagram for the experimental steel calculated using JMatPro software

optical and SEM micrographs of TMCP samples cooled down either by AC or WQ. All the specimens reveal bainite in dark contrast and martensite in bright contrast. The higher amount of bainite in air-cooled samples is attributed to the higher bainitic hardenability, achieved due to the alloy design of the proposed steel as shown in Fig. 3(a, c and e). It is evident that the martensite was obtained during air cooling in the present steel (in spite of its low carbon content) due to the alloying additions shifting the nose of transformation curve to the right, increasing the hardenability of austenite. However, in large-size engineering component, variation in the amount of martensite between the core and surface structure of steel is expected due to the difference in cooling rate at those regions during air cooling (core cools at a slower rate than the surface). Still, air cooling is preferred due to the generation of lower residual stress and stress gradient as compared to water quenching. On the other hand, a lesser amount of bainite and a significant amount of martensite are obtained in WQ, as shown in Fig. 3(b, d and f), which is expected due to the higher cooling rate of water quenching. As a consequence, austenite is directly converted primarily to martensite, avoiding bainitic transformation. Bainite laths having fine carbides are revealed in the SEM micrograph at the inset of Fig. 3(a). The martensite and bainite laths are intersected each other in SEM micrograph at the inset of Fig. 3(d).

It is noteworthy that average grain diameter has been considered for equiaxed and irregular grains, whereas average width has been used for elongated grains to calculate prior austenite grain (PAG) size, Fig. 3(e). SEM micrograph at the inset of Fig. 3(f) indicates parallel martensitic laths. In the present study, hot rolling makes PAGs to be elongated along the rolling direction, which is normally considered as the nucleating site for bainitic ferrite. The average pancaked austenite grain size lies in the range of 35-45 μm for AC samples and 30-40 μm for WQ specimens. It is evident that the microstructural evolution is almost similar in the chosen range of FRT, Fig. 3(a, b, c, d, e and f). However, average grain size reduces with the decrease in FRT for both the cooling conditions. In addition, the grain sizes of AC samples are greater than the WQ samples irrespective of FRTs. It is obvious that the laths of bainite/martensite are finer in WQ and lower FRT condition due to faster cooling and higher deformation at a lower temperature. Such kind of grain refinement is beneficial to increase the strength and toughness (Ref 31). It is evident that austenite grains become flattened (pancaked shape) during TMCP which causes accumulation of dislocations and other crystalline defects such as deformation bands and twins inside the austenite grain (Ref 32). Such type of pancaked austenite promotes grain/lath refinement during the transformation from austenite to bainite/martensite.

3.2 Transmission Electron Microscopy

Transmission electron microscopy was conducted to study the intricate microstructural features. Figure 4(a, b, c, d, e and f) shows the bright-field (BF) electron image of the steel rolled at various FRTs and cooled by AC (a, c and e) or WQ (b, d and f). Figure 4(a and b) of AC samples processed at 850 °C FRT primarily shows lower bainite along with lath martensite. Bainite is an aggregate of cementite and ferrite laths containing a high density of dislocations. Figure 4(b) reveals predominantly martensite and lower bainite with high dislocation density in WQ samples. Figure 4(c) for the sample processed at
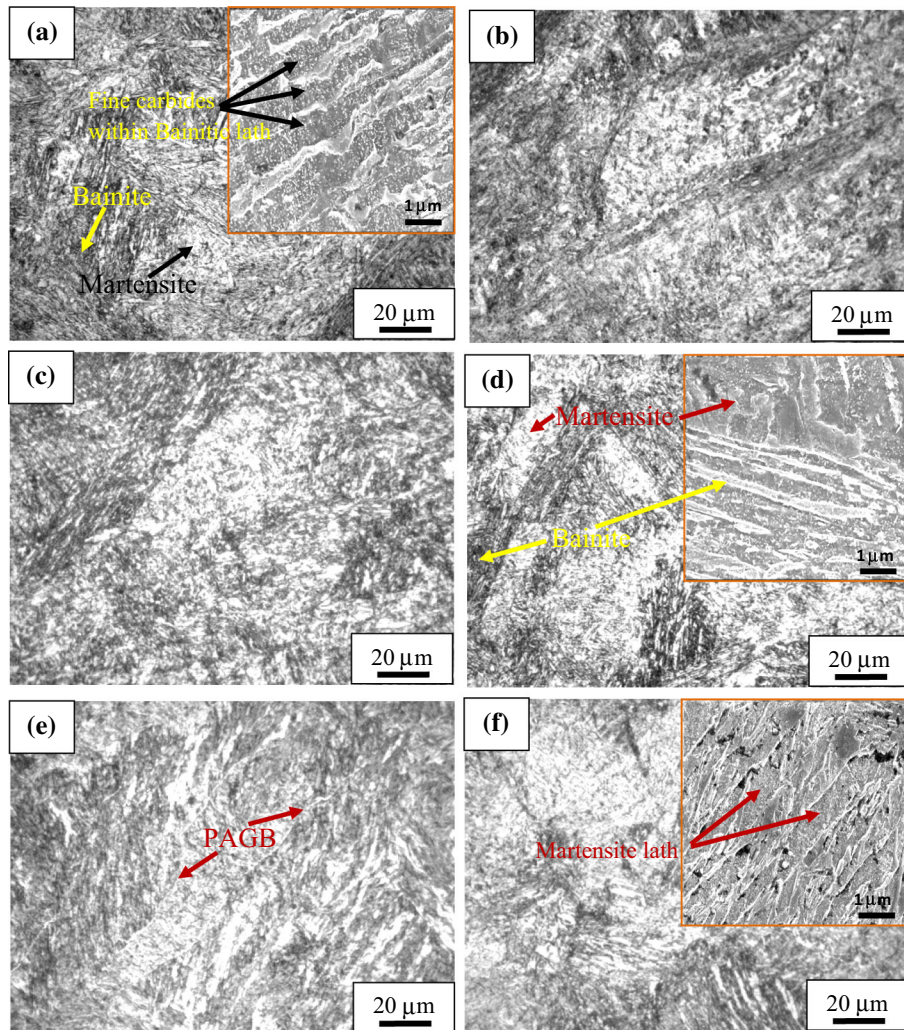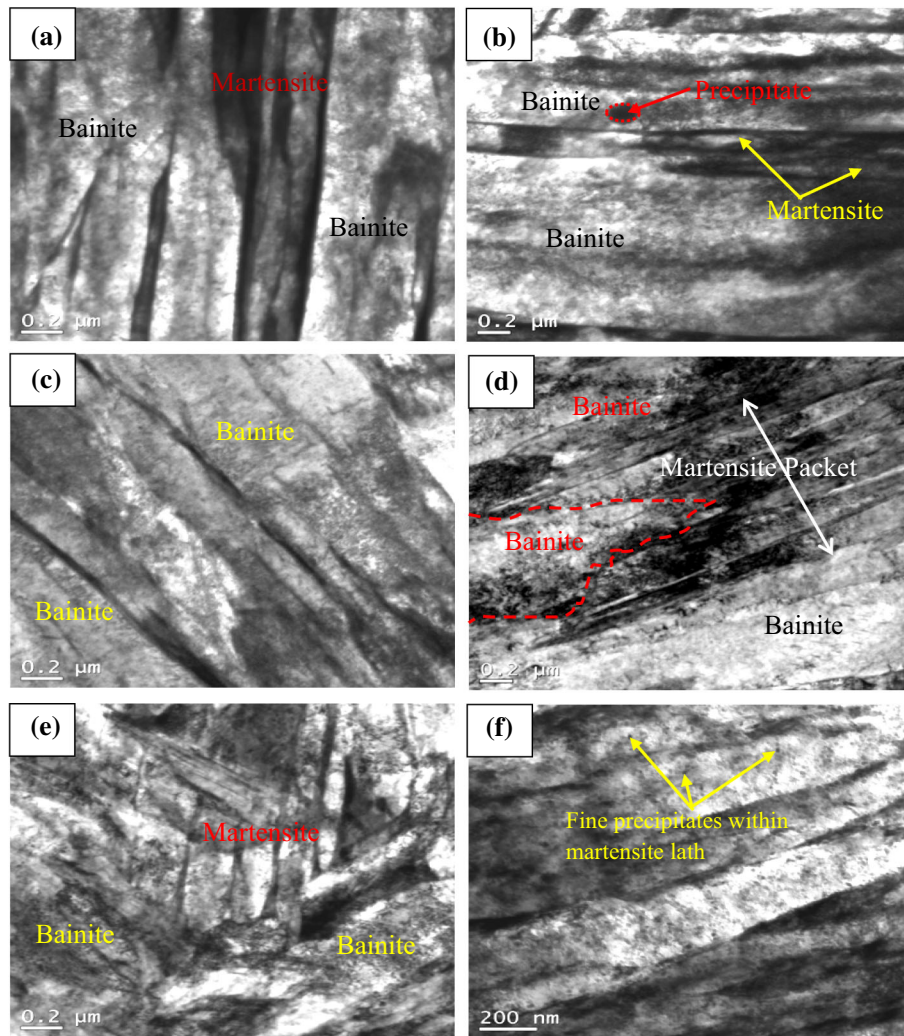
Fig. 3 Optical and SEM micrographs of the investigated steel subjected to TMCP followed by AC (a, c, e) and WQ (b, d, f). Steel processed at (a, b) 850 °C FRT, (c, d) 800 °C FRT and (e, f) 750 °C FRT, respectively, PAGB—prior austenite grain boundary

800 °C FRT followed by AC demonstrates lower bainite consisting of plate-like ferrite with fine carbide and fine precipitates inside the bainitic ferrite lath. Figure 4(d) for the sample of the same FRT followed by WQ shows the mixed bainite–martensite structure. It is evident that the cluster of the martensite laths is observed in parallel and one particular orientation which are generally termed as martensite packet. Figure 4(e) also exhibits the mixture of bainite plate and lath martensite, processed at 750 °C FRT and AC. It is indicating that bainite/martensite packets are penetrated into each other. The martensite laths are adjacent to lower bainite due to the accommodation strain. The formation of martensite lath is suppressed by the surrounding bainite, and thereby, the martensite laths are shortened. Figure 4(f) shows a mixture of bainite plate and lath martensite, processed at 750 °C FRT and WQ.

It is evident from all the TEM bright-field images presented in Fig. 4 that the samples comprise mixed microstructural constituents of bainite and martensite. The bainite laths/plates in AC samples are coarser than those in the WQ samples for different FRTs. The dark portion in between the two laths of bainite/martensite is difficult to resolve which can be due to their mutual accommodation strain. The high-density disloca-

tion networks and dislocation tangles inside the bainitic laths contribute additional strength. The abundant planar array of dislocations and dislocation node–precipitate interaction are the other strengthening factors (Ref 33).

TEM bright-field image of 850 °C FRT, AC sample in Fig. 5(a) shows the fine precipitates and discontinuous carbides within the bainitic structure. Bright-field TEM image in Fig. 5(b) demonstrates a lower bainite with high dislocation density in 800 °C FRT, AC sample, and the corresponding dark-field image given as inset indicates the presence of retained austenite (RA). The selected area electron diffraction (SAED) pattern and its schematic analysis at the inset of Fig. 5(b) confirmed the presence of RA. During rolling, 'deformation-induced' plentiful dislocation arrays and dislocation nodes could act as the preferred nucleation sites for the precipitates. Figure 5(c) reveals very fine martensite (ε-martensite) laths to the level of 4-5% adjacent the bainite plate obtained at 800 °C FRT, WQ sample. It is apparent that the formation of lath martensite is restricted by the adjacent bainite. Such an accommodation of strain increases the residual stress and contributes additional strengthening. The SAED pattern at the inset of Fig. 5(c) indicates the presence of α′- and ε-martensite laths surrounding the bainite plate. During TMCP at

Fig. 4 TEM bright-field (BF) image of the investigated steel specimen subjected to TMCP followed by AC (a, c, e) and WQ (b, d, f). Steel processed at (a, b) 850 °C FRT, (c, d) 800 °C FRT and (e, f) 750 °C FRT, respectively

a lower temperature, extensive heterogeneous deformation results in the formation of shear bands which act as the potential nucleation sites for α′-martensite formation. On the other side, in low stacking fault energy (SFE) region, stacking faults frequently form and their overlapping promotes the nucleation of ε-martensite. Figure 5(d) shows the discontinuous carbide formation within the bainitic ferrite plate in the sample processed at 750 °C FRT, AC. It is worth mentioning that nano-sized fine precipitates offer grain refinement (or the stabilization of the fine lath structure) by the pinning action to the grain boundary migration. Therefore, the grain refinement and the dislocation–precipitate interactions are basically the two phenomena which contribute significantly to ultrahigh-strength level in the present steel. TEM bright-field image in Fig. 5(e) of 800 °C FRT, AC sample exhibits nearly round precipitates (30-40 nm) within the bainite plate. The EDS spectrum in Fig. 5(f) taken from these particles reveals that those are rich in Cu, possibly (Cu, Ni) Fe-type precipitates. Generally, irrespective of the nature of the copper precipitates formed during the decomposition of austenite, the different morphologies such as spherical, irregular triangular and oblong usually occur at 750-500 °C temperature after hot rolling followed by air cooling or ageing at that temperature range (Ref 34, 35). Apart from Cu,

the other elements picked up in the EDS analysis given in Fig. 5(f) can come from the matrix. Hence, the chemistry of the precipitates is complex, but is reasonable to consider those as Cu-rich precipitates. Therefore, the investigated steel has exploited the benefit of Cu addition in conjunction with Ni.

Figure 6(a) shows the fine ($\approx$ 70 nm) spherical NbC precipitate (identified from the EDS in Fig. 6b) within the bainite plate of 850 °C FRT-AC sample. Figure 6(c) indicates fine ($\approx$ 65 nm) and irregular-shaped TiC/TiCN particle (identified from EDS in Fig. 6d) inside the martensite lath with high dislocation density in the sample of 800 °C FRT followed by WQ. Figure 6(e) shows the presence of fine ($\approx$ 55 nm) and nearly spherical MoC precipitate (identified from the EDS analysis in Fig. 6f) within the lower bainite, containing high dislocation density, in the sample WQ from 750 °C FRT. The formation of the above-mentioned precipitates at different temperature range is verified by the Thermo-Calc® software with the TCFE7 thermodynamic database. Figure 7 presents the increase in volume fractions of various precipitates in the investigated steel upon equilibrium cooling from 1500 to 400 °C as predicted by Thermo-Calc® software. It is evident from Fig. 7 that the precipitation sequence during cooling is TiN (starts $\sim$ 1500 °C), followed by NbC (starts $\sim$ 1300 °C),
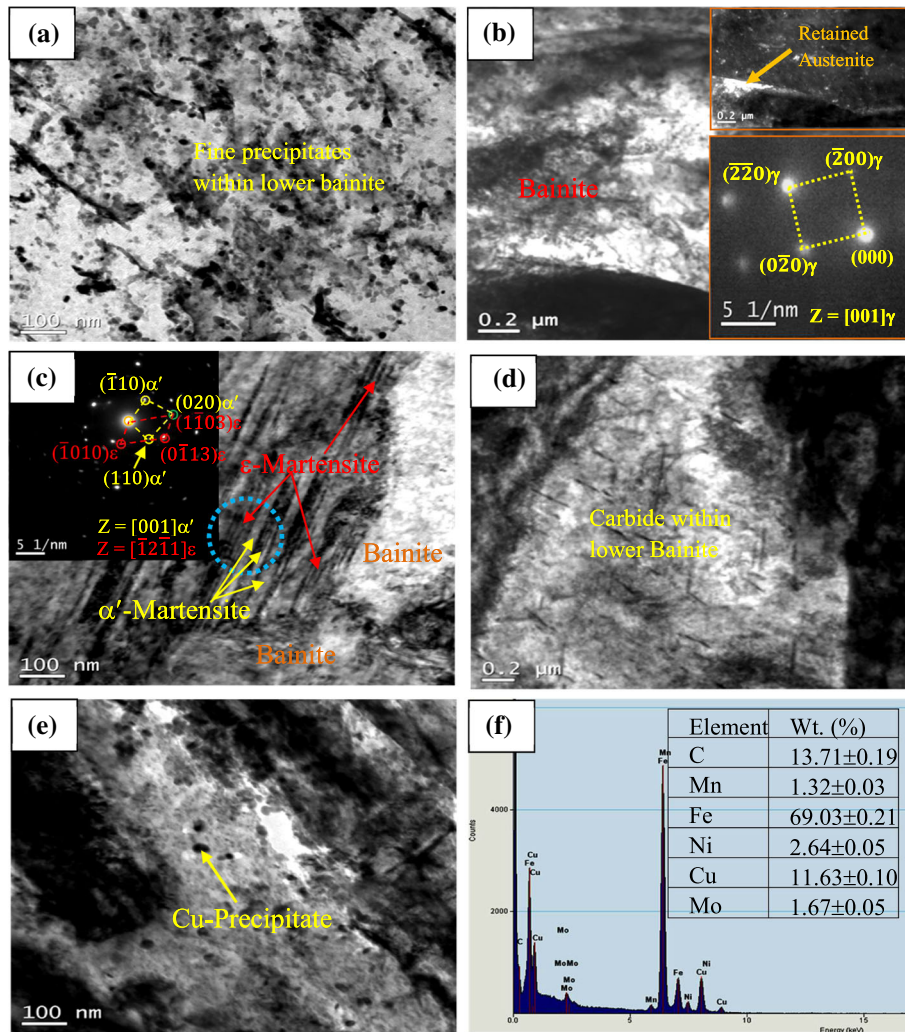
Fig. 5 (a) Fine precipitates and discontinuous carbide within bainitic structure at 850 °C FRT-AC, (b) lower bainite with high dislocation density after air cooling from 800 °C FRT and the dark-field image of the corresponding bright-field image in inset and its SAED analysis, (c) very fine martensite lath adjacent the bainite plate obtained at 800 °C FRT followed by WQ. (d) Discontinuous carbide within bainitic ferrite plate obtained after 750 °C FRT-AC. (e) Cu-rich precipitate within bainite plate obtained at 800 °C FRT followed by AC and (f) the corresponding EDS spectrum, respectively

whilst MoC and Cu-rich precipitates form at a lower temperature (600-700 °C). The volume fractions of both MoC and Cu precipitates are predicted to be much higher than of the TiN and NbC precipitates. Due to water quenching after rolling, the precipitate size in WQ samples is often too fine to be detected. Further analysis of the TEM micrographs indicates that the particle size becomes finer with the decrease in FRT and the increase in cooling rate. Finer precipitates restrict the dislocation movement more effectively in WQ samples than that in AC samples. Consequently, the WQ specimens have higher precipitation strengthening in addition to martensitic strengthening as compared to the AC samples.

### 3.3 Crystallographic Texture and Grain Boundary Misorientation Analysis

Figure 8(a, b, c, d, e and f) represents the normal direction–inverse pole figure (ND-IPF) colour maps showing the crystal orientations along the normal direction of the air-cooled and water-quenched samples following the colour code given in Fig. 8(g). IPF maps obtained from the EBSD analysis show the dominance of Goss and rotated Goss textures (green-coloured regions) having <110>//ND, i.e. {110} planes parallel to the rolling plane, Fig. 8. Some amount of gamma fibre-textured regions (in blue) with <111>//ND and cube-textured regions (in red) with <001>//ND can also be seen in Fig. 8.

Figure 9(a, b, c, d, e and f) exhibits the orientation distribution function (ODF) within the $\phi_2 = 45°$ section of the Euler space for all the processed samples as obtained from the EBSD analysis. Figure 9(g) presents the standard $\phi_2 = 45°$ ODF section showing the texture components typically found in ferritic (BCC) steel (Ref 36). The dominance of Goss, {110} <001>, and rotated Goss, {110} <110>, texture components also becomes evident from the ODF sections in Fig. 9. The texture was quite random in nature at 850 °C FRT samples, especially in 850 °C AC sample, Fig. 9(a). The 850 °C-WQ sample had a strong intensity near alpha-fibre orientation ({112} <110>), shifted from its ideal position, Fig. 9(b). The Goss-type textures intensified with the decrease in FRT to 800 °C and finally to 750 °C. This can be attributed to the higher strain accumulation and greater pancaking of prior
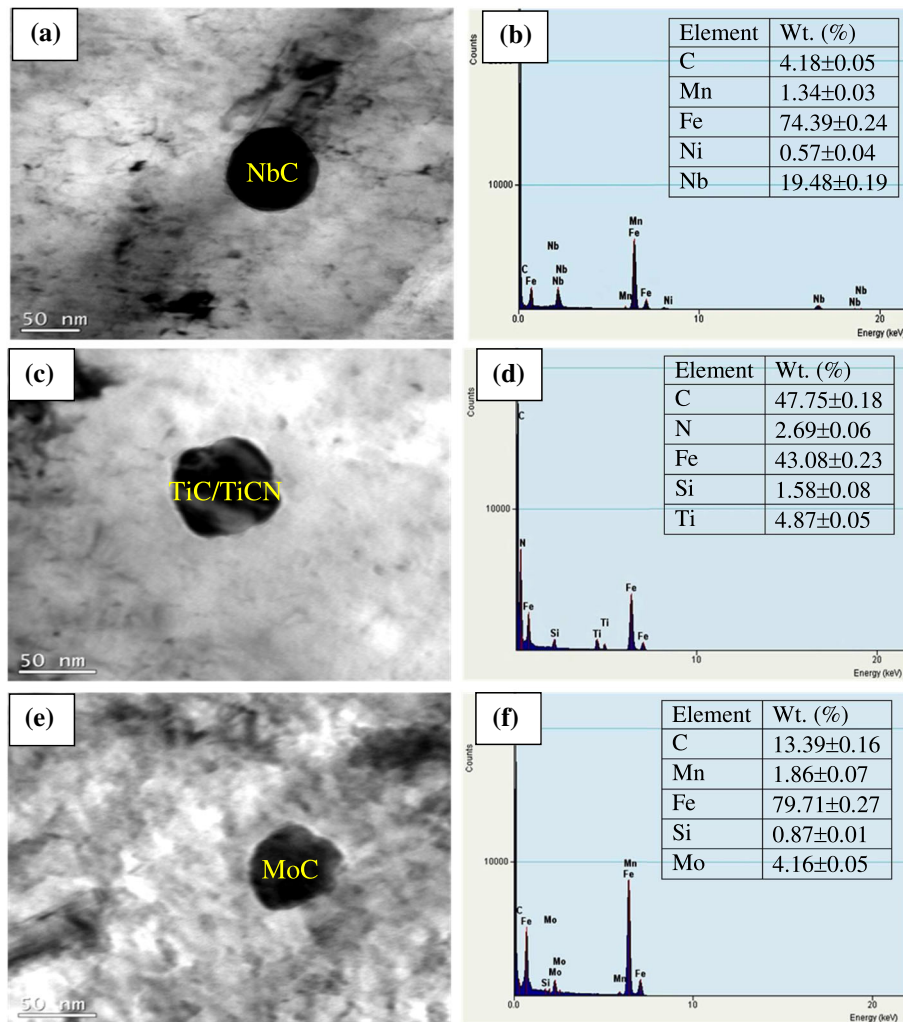
Fig. 6 TEM image showing (a) fine spherical precipitate within bainite plate at 850 °C FRT-AC, (c) fine irregular-shaped particle inside the martensite lath at 800 °C FRT-WQ, (e) fine precipitate within lower bainite with high dislocation density at 750 °C FRT-WQ. (b), (d) and (f) showing their EDS spectra indicating NbC, TiC/TiCN and MoC precipitates, respectively
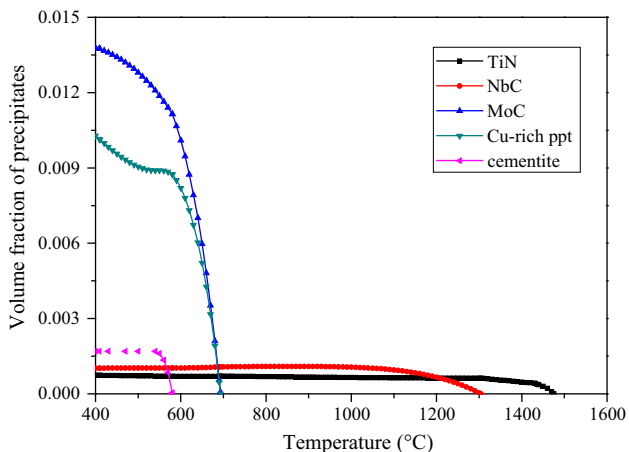

Fig. 7 Volume fraction of precipitates as a function of temperature calculated by Thermo-Calc® software

austenite grain structure at lower FRT which promoted the variant selection (i.e. preferential formation of Goss type variants) during the phase transformation upon cooling

(Ref 37). As the deformed austenite transforms into bainite or martensite, depending on the severity of deformation with the associated deformed microstructure and texture of austenite along with the cooling rate employed during transformation, the formation of certain crystallographic variants (following an established orientation relationship like Kurdjumov–Sachs (KS) orientation relationship) is favoured. Such a variant selection occurs in order to accommodate the transformation-induced dilation and shear strains. Besides Goss orientation, ODF sections also show the existence of Brass texture, i.e. {110} <112>, in the samples deformed at lower FRT (800-750 °C). Overall <110>//ND emerged as the dominant texture. As mentioned above, the IPF maps further indicate the presence of limited extent of other fibre orientations like gamma fibre, <111>//ND (depicted by 'blue'), and cube, <001>//ND (depicted by 'red') textures. These findings are consistent with the texture evolution in low-carbon HSLA steels with bainitic and martensitic microstructures (Ref 38).

Misorientation across the various boundaries present within the microstructures of the present steel was also studied from the EBSD analysis. The intensity of low-angle boundaries (2°-15° misorientations) was higher (60-65%) as compared to the
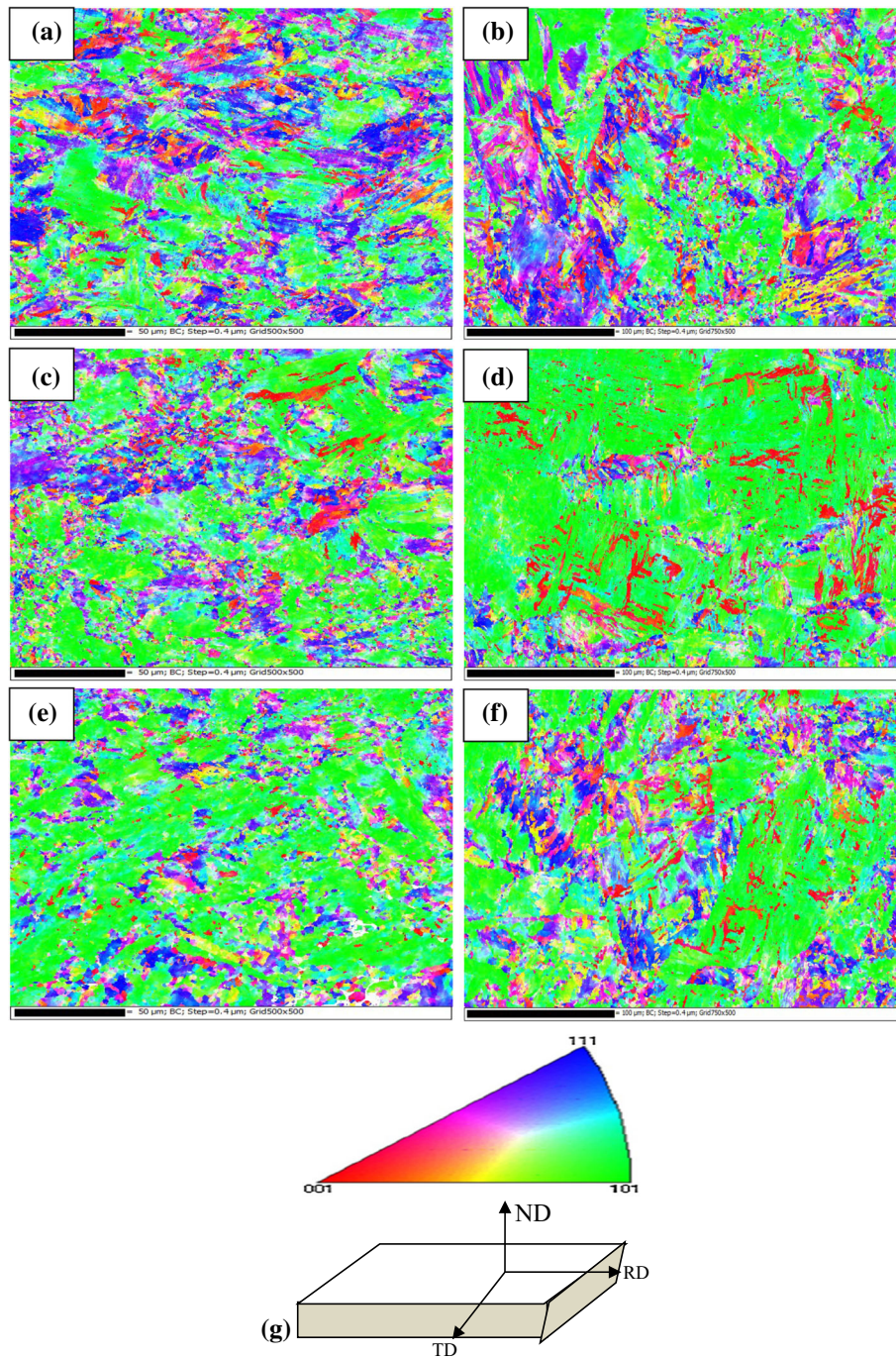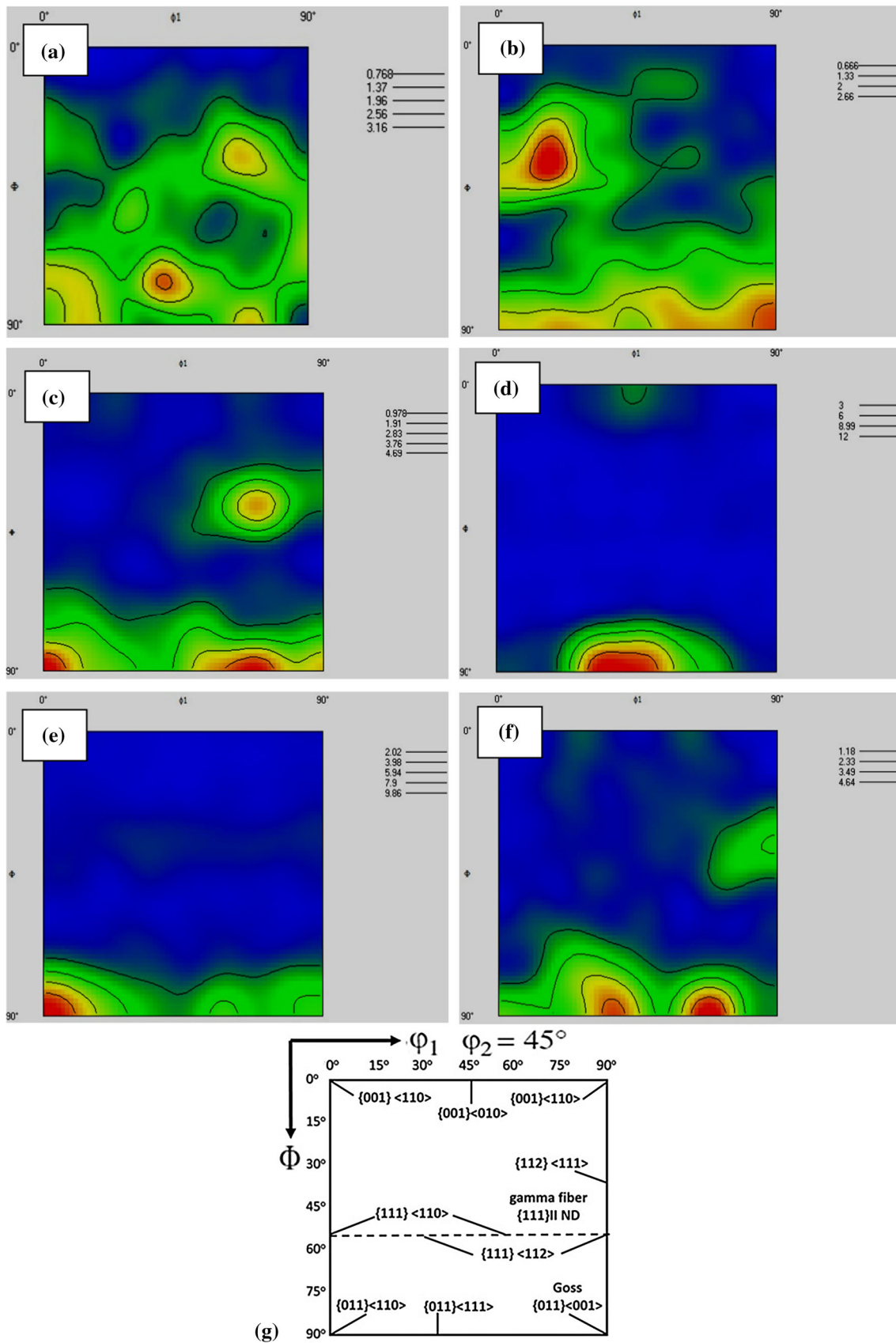
Fig. 8 ND-IPF maps obtained from EBSD analysis of (a, c, e) air-cooled and (b, d, f) water-quenched samples: (a, b) 850 °C FRT, (c, d) 800 °C FRT, (e, f) 750 °C FRT and (g) unit triangle of IPF showing the crystal alignment with respect to the normal direction (ND) of the samples. ND, RD and TD stand for normal direction, rolling direction and transverse direction, respectively

high-angle boundaries ($> 15°$). The high intensity of low-angle boundaries is certainly expected in bainitic and martensitic microstructures as those include 'intra-lath' dislocation substructures and lath boundaries (Ref 39). On the contrary, the high-angle boundaries are primarily the packet boundaries and prior austenite grain boundaries (Ref 40). It is reported that in the presence of bainitic laths and martensite-austenite (M-A) films, the lath boundaries can also act as the high-angle boundaries (Ref 41).

3.4 Hardness and Tensile Properties

Figure 10 shows the engineering stress–strain diagrams of AC and WQ samples. Table 2 summarises the mechanical properties of all the investigated samples. The tensile curves represent a continuous yielding behaviour which can be attributed to the bainitic and martensitic microstructure (not ferrite–pearlite) having plenty of mobile dislocations (Ref 42). Higher hardness, yield strength (YS) and ultimate tensile

Fig. 9 $\phi_2 = 45°$ ODF sections obtained from EBSD analysis for (a, c, e) air-cooled and (b, d, f) water-quenched samples: (a, b) 850 °C FRT, (c, d) 800 °C FRT, (e, f) 750 °C FRT and (g) standard $\varphi_2 = 45°$ ODF section of the Euler space showing the locations of ideal orientations for ferritic (BCC) steel

strength (UTS) and lower elongation are achieved in WQ specimens than those in AC specimens. Uniform elongation (UEL) and total elongation (TEL) of AC samples are higher than those of WQ samples. The higher strength and lower ductility in WQ samples can be attributed to fine lath martensitic structure, high dislocations density and dislocation–precipitate interaction as mentioned earlier. It has been observed that hardness, YS and UTS increase in AC condition with the reduction in FRT. In contrast, under WQ, the sample processed at the highest FRT of 850 °C yields the maximum UTS. However, ductility remains almost the same which can be a consequence of grain/lath refinement. The sample with the lowest FRT of 750 °C, followed by WQ, gives the maximum hardness of about 543 HV, and the sample processed at 850 °C FRT followed by AC gives the minimum hardness of about 453 HV. The sample with 750 °C FRT followed by WQ gives the maximum YS of 1449 MPa and UTS of 1669 MPa. The specimen with FRT 750 °C has exhibited the best combination of strength, ductility and static tensile toughness (TT). Phase transformation of austenite to martensite/bainite plays a crucial role in strengthening. The ultrahigh-strength level of the developed steel is substantiated with fine, microalloy precipitates, discontinuous carbides and high dislocation density inside the lath microstructures.

3.5 Impact Toughness and Fractographic Analyses

The variation in impact toughness with testing temperatures of AC and WQ samples processed at different FRTs is presented in Table 3. The sample processed at 750 °C FRT
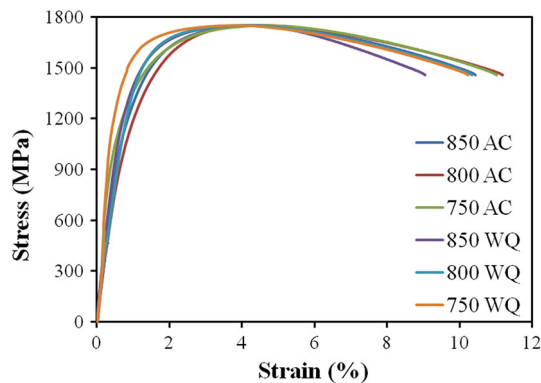
followed by AC yields the maximum impact toughness at room temperature (RT) and minimum at − 40 °C. However, it is observed that the impact toughness values of AC specimens at RT are higher than those of WQ specimens. On the other hand, impact toughness values of AC specimens at − 40 °C are lower than those of WQ specimens. At room temperature and at − 40 °C, the impact toughness is almost within a close range for both the cooling conditions. The main variation in impact toughness occurs between room temperature and sub-zero temperature for a particular cooling condition. It is evident that the TMCP specimens exhibit good impact toughness at sub-zero temperature, which is necessary for the structural applications under cold weather conditions. In general, finish rolling at relatively lower temperature developed finer grain sizes, fine precipitates along with the dominant Goss and rotated Goss texture components (having $<110>//ND$). These factors in combination permitted the steel plate to reach a good combination of strength and toughness.

Figure 11(a, b, c and d) illustrates the fracture surfaces of the specimens processed at 750 °C FRT, AC, impact tested at room temperature and 850 °C FRT, WQ, impact tested at − 40 °C. The fracture surfaces demonstrate a mixture of microvoids, small spider-net like dimples and also some shear lips. The formation of dimples ensures the ductile nature of the fracture contributing to the high impact toughness by absorbing plastic strain during the void growth, before the coalescence of microvoids. 750 °C FRT, AC specimen shows the fine dimples which contributed to the maximum impact toughness at room temperature. The fracture surface of 850 °C FRT-WQ specimen tested at sub-zero temperature is flatter; dimples are larger and shallower, and some cleavage facets are also present. These indicate to the nature of quasi-cleavage fracture in 850 °C FRT, WQ. It is obvious that the impact toughness associated with a

Fig. 10 Engineering stress–strain diagram of TMCP specimens with FRT range of 850-750 °C followed by air cooling (AC) and water quenching (WQ)

Table 3 Charpy impact properties (2 mm "V" notched sample)

	Impact toughness (in J)	
FRT, °C	(+) 20 °C or room temperature (RT)	(−) 40 °C
Air-cooled steel		
850	24 ± 1	20 ± 1
800	28 ± 2	20 ± 1
750	30 ± 2	18 ± 1
Water-quenched steel		
850	24 ± 1	20 ± 1
800	26 ± 1	22 ± 1
750	23 ± 1	20 ± 1

Table 2 Hardness and tensile properties under various processing conditions

FRT, °C	Hardness, HV	YS, MPa	UTS, MPa	UEL, %	TEL, %	TT, MPa
Air-cooled steel						
850	453 ± 5	1034 ± 5	1598 ± 7	5.70 ± 1	12.57 ± 1	113 ± 2
800	481 ± 4	1124 ± 6	1610 ± 4	5.41 ± 1	12.83 ± 1	116 ± 2
750	506 ± 8	1149 ± 8	1662 ± 6	5.64 ± 1	13.64 ± 2	130 ± 3
Water-quenched steel						
850	510 ± 8	1225 ± 5	1726 ± 7	4.37 ± 1	10.03 ± 1	100 ± 2
800	528 ± 6	1414 ± 7	1616 ± 5	2.38 ± 1	10.50 ± 1	101 ± 4
750	543 ± 6	1449 ± 4	1669 ± 8	3.68 ± 1	10.78 ± 1	102 ± 3
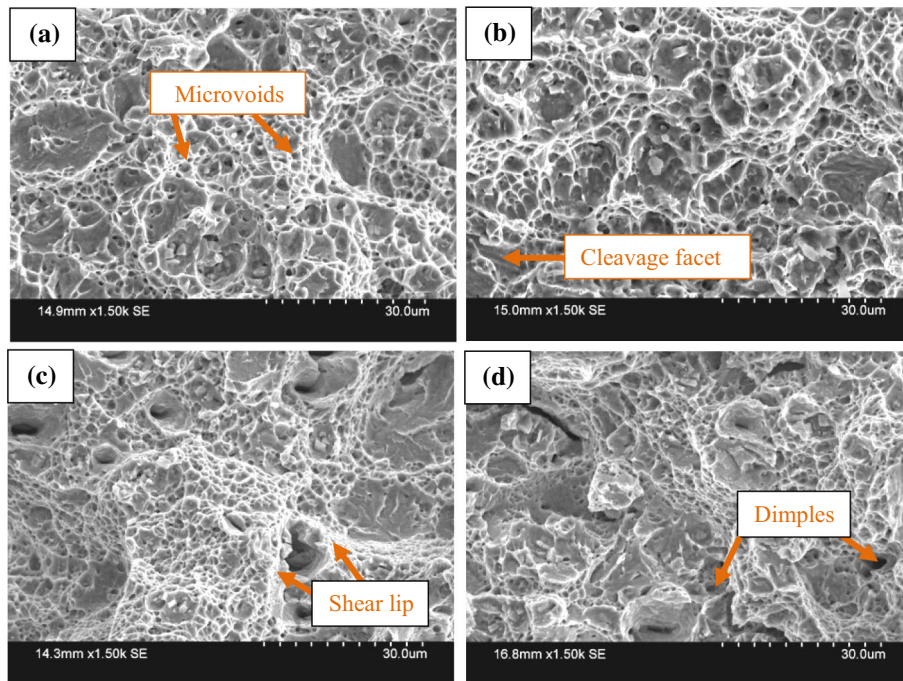
Fig. 11 Fracture surfaces of 750 °C FRT and air-cooled samples tested at (a) room temperature and (b) sub-zero temperature (− 40 °C); (c) sample with 850 °C FRT followed by water quenching tested at (c) room temperature and (d) sub-zero temperature (− 40 °C)

quasi-cleavage fracture is lower than that of ductile rupture due to its relatively lower plastic strain during crack initiation and propagation (Ref 43).

3.6 Discussion on the Composition, Microstructure, Texture and Properties

As mentioned earlier, extensive studies have been carried out for the past two decades on the development of HSLA steels with the addition of Cu and Ni (Ref 44-46). In general, these steels contain low-C (0.04-0.13 wt.%), Ni up to 4%, Cu up to 2%, along with the additions of Mo, Cr and the microalloying elements (V, Nb, Ti) at different proportions. A wide range of YS (700-1300 MPa), UTS (800-1400 MPa), elongation to failure (10-30%) and Charpy impact toughness (5 J at ambient temperature to 100 J at − 80 °C) were obtained in those studies. The steels in general finish rolled over 900-1000 °C, cooled in air, oil, water-quenched, and aged over the range of 500-600 °C. Besides precipitation strengthening, Cu precipitates act as [H] traps and improve the hydrogen induced cracking resistance (Ref 46). Cu precipitates also do not hamper the toughness by allowing dislocation to climb over or bow around them (avoiding intense dislocation pile-up) (Ref 34).

Co-precipitation of Cu along with other precipitates, such as microalloy carbides and carbonitrides, Mo_2C, $(Ti, Mo)_2C$, $(Nb, Mo)C$, not only provides significant strengthening, but also ensures the microstructural stability if there is a risk of Cu precipitate coarsening (Ref 46). Heterogeneous nucleation of M_2C carbides (where M represents Cr, Mo and Ti) on the Cu precipitates was also reported (Ref 47). Such a possibility can explain the observation of Cu-rich complex precipitates observed in Fig. 5. The presence of Ni and Cu along with Mn and Al was found to form B2-intermetallic precipitates (BCC) in high-strength steels (Ref 45). The effect of finish deformation temperature on precipitation strengthening during final cooling and ageing treatment can be complex. Gladman

preferred low-temperature deformation of austenite to achieve a pancake structure for increasing the precipitation strengthening during final cooling (and ageing treatment) (Ref 6). In this case, high dislocation density in the transformed microstructure inherited from the high-temperature deformed structure, expected to provide the nucleation sites for precipitation after transformation. On the other side, Gornia and Mei (Ref 44) recommended applying high-roughing deformation and low-finishing deformation for utilising the benefit of precipitation strengthening at lower temperatures. As the austenite recrystallises immediately after deformation, it restricts high-temperature precipitation during deformation and encourages the precipitation to take place during final cooling (or ageing treatment) in fine scale at relatively lower temperatures where there is a less scope for precipitate growth. In the present study, although hardness and strength increase with the decrease in FRT (verifying the statement of Gladman) (Ref 6), in certain cases high hardness or strength is obtained at high FRT of 850 °C. Such an observation can be explained by the above-mentioned finding of Gornia and Mei (Ref 44). As both Ni and Cu are austenite stabilisers, their effect on the phase transformation during cooling and especially in the formation of retained austenite/M-A constituent is crucial. Although retained austenite can provide transformation-induced plasticity (TRIP) effect (Ref 48), their transformation into fresh, un-tempered martensite can impart brittleness. Although such a detrimental effect is not observed in the present study, still there can be a contribution of martensitic transformation to the cleavage fracture of 850 °C FRT, WQ sample at low temperature.

TEM study and Thermo-Calc® software prediction indicated to the precipitations of TiN, NbC, Mo- and Cu-containing precipitates. TiN is known to prevent the austenite grain growth during soaking treatment. The strain-induced precipitation of NbC resists the austenite recrystallisation during thermomechanical controlled rolling (by interacting with the dislocations) and thereby contributes to the grain refinement. Lastly, MoC

and Cu precipitations at a lower temperature and at a fine scale are expected to provide precipitation strengthening to the steel. Although the laboratory scale non-equilibrium processing can suppress the precipitation temperature and fraction to some extent as predicted from Thermo-Calc®, the precipitation sequence and the nature of the precipitates are expected to remain the same.

Finally, the effect of crystallographic texture, dominated by $<110>$//ND orientations, on the strength-toughness combination needs to be discussed. {110} planes are the primary slip planes in BCC. Having those planes parallel to the sheet surface (i.e. rolling plane) can decrease the resolved shear stress on those planes during tensile or compressive loading. That is expected to contribute a texture strengthening effect as slip has to occur by the activation of secondary slip systems. {100} planes act as the cleavage planes in BCC as cleavage cracks propagate through those planes having low cohesive strength. $<110>$//ND texture ensures that {100} planes remain inclined (preferably at 45°) to the main fracture plane of the impact test specimens. As a result, there was a high resistance to cleavage fracture as the crack has to follow a more tortuous path, rather than propagating easily along the flat fracture plane. As a result, cleavage cracking is resisted at sub-zero test temperature, and fracture happened by a mixed mode combining both ductile and cleavage mechanisms, i.e. quasi-cleavage fracture.

4. Conclusions

A novel low-carbon Cu-Ni-Mo-Ti-Nb steel has been developed through TMCP processing with two different cooling routes (AC and WQ) without any post-heat treatment for achieving attractive mechanical properties. The most important findings are listed below:

1. Water-quenched samples show a higher amount of martensite constituent resulting in higher strength and lower tensile toughness in contrast to air-cooled samples.
2. The microstructure becomes gradually finer with the lowering of FRT, irrespective of cooling conditions which results in good elongation and toughness. However, the bainite lath is wider in AC samples than WQ specimens owing to slower cooling.
3. Ti-Nb-Mo- and Cu-enriched nano-scale precipitate particles have been developed in both AC and WQ specimens, interacting with the dislocations and substructures, ensuing ultrahigh-strength level during TMCP.
4. Intensification of the Goss and rotated Goss texture components has strengthened the samples by a texture strengthening effect and resisted the cleavage fracture at the sub-zero test temperature. The decrease in FRT and the increase in cooling rate increased the fraction of large misorientation grain boundaries, which resisted the crack propagation and improved the impact toughness.
5. The proposed composition and processing schedule achieved an ultrahigh level of yield strength ($\approx$ 1232 MPa), tensile strength ($\approx$ 1647 MPa) and reasonable total elongation ($\approx$ 12%) along with a satisfactory low-temperature ($-$ 40 °C) impact toughness ($\approx$ 20 J) through an appropriate alloy design and optimised TMCP parameters without any extra heat treatment.

References

1. T.V. Philip and T.J. McCaffy, *Ultrahigh Strength Steel*, Tenth edition, ASM International, USA, Metals Handbook, 1990, p 431–448
2. J.G. Speer, D.K. Matlock, B.C. De Cooman, and J.G. Schroth, Carbon Partitioning into Austenite After Martensite Transformation, *Acta Mater.*, 2003, **51**(9), p 2611–2622
3. H.K.D.H. Bhadeshia, *Bainite in Steels*, 2nd ed., IOM Communications, London, 2001
4. H.K.D.H. Bhadeshia, Large Chunks of Very Strong Steel, *Mater. Sci. Technol.*, 2005, **21**, p 1293–1302
5. G. Caballero, C. Garcia-Mateo, and M.K. Miller, Modern Steels at Atomic and Nanometre Scales, *Mater. Sci. Technol.*, 2015, **31**, p 764–772
6. T. Gladman, *The Physical Metallurgy of Microalloyed Steels*, London, UK, Institute of Materials, 1997, p 240
7. H.K.D.H. Bhadeshia and R. Honeycombe, *Steels: Microstructure and Properties*, 3rd ed., Elsevier Ltd., Amsterdam, 2006, p 221
8. R. Kuziak, R. Kawalla, and S. Waengler, Advanced High Strength Steels for Automotive Industry, *Arch. Civ. Mech. Eng.*, 2008, **8**, p 103–117
9. M. Zhao, K. Yang, and Y. Shan, The Effects of Thermo-Mechanical Control Process on Microstructures and Mechanical Properties of a Commercial Pipeline Steel, *Mater. Sci. Eng. A*, 2002, **335**, p 14–20
10. S. Mandal, N.K. Tewary, S.K. Ghosh, D. Chakrabarti, and S. Chatterjee, Thermo-Mechanically Controlled Processed Ultrahigh Strength Steel: Microstructure, Texture and Mechanical Properties, *Mater. Sci. Eng. A*, 2016, **663**, p 126–140
11. T. Heller, B. Engl, G. Stich, and G. Thiemann, in *Proc. Int. Conf. TMP' 2000 London*, London, (2000), p. 438
12. F.B. Pickering, *Physical Metallurgy and the Design of Steels*, Applied Science Publishers, London, 1978, p 101–126
13. A. Takahashi and M. Iino, Microstructural Refinement by Cu Addition and Its Effect on Strengthening and Toughening of Sour Service Line Pipe Steels, *ISIJ Int.*, 1996, **36**, p 241–245
14. A.J. Craven, K. He, L.A.J. Garvie, and T.N. Baker, Complex Heterogeneous Precipitation in Titanium-Niobium Microalloyed Al-Killed HSLA Steels-I (Ti, Nb) (C, N) Particles, *Acta Mater.*, 2000, **48**, p 3857–3868
15. R.D.K. Misra, G.C. Weatherly, J.E. Hartmann, and A.J. Boucek, Role of structure and microstructure in the enhancement of strength and fracture resistance of ultra-high strength hot rolled steels, in *42nd MWSP Conference Proceedings ISS*, vol. 38 (2000) pp. 391–405
16. H. Kejian and T.N. Baker, The Effects of Small Titanium Additions on the Mechanical Properties and the Microstructures of Controlled Rolled Niobium-Bearing HSLA Plate Steels, *Mater. Sci. Eng. A*, 1993, **169**(1–2), p 53–65
17. S. Tirnanic, R. Curcic, D. Tirnanic, and D. Drobnjak, Properties of Thermo-Mechanically Rolled Nb/Ti Micro-alloyed Steel Sheets, *Steel Res.*, 1989, **60**, p 561–565
18. Y. Funakawa, T. Shiozaki, K. Tomita, T. Saito, H. Nakata, K. Sato, M. Suwa, T. Yawamoto, Y. Murao, and E. Maeda, *Patent on High Strength Hot Rolled Steel Sheet and Method of Manufacturing the Same*, Pub. No.: US 2003/0063996 A1
19. F.B. Pickering and B. Garbarz, Strengthening in Pearlite Formed from Thermo-Mechanically Processed Austenite in Vanadium Steels and Implications for Toughness, *Mater. Sci. Technol.*, 1989, **5**, p 227–237
20. S. Mukherjee, I.B. Timokhina, C. Zhu, S.P. Ringer, and P.D. Hodgson, Three-Dimensional Atom Probe Microscopy Study of Interphase Precipitation and Nanoclusters in Thermomechanically Treated Titanium-Molybdenum Steels, *Acta Mater.*, 2013, **61**, p 2521–2530
21. S. Zhang, P. Wang, D. Li, and Y. Li, Investigation of the Evolution of Retained Austenite in Fe-13%Cr-4%Ni Martensitic Stainless Steel During Intercritical Tempering, *Mater. Des.*, 2015, **84**, p 385–394

22. Z.B. Jiao, J.H. Luan, M.K. Miller, and C.T. Liu, Precipitation Mechanism and Mechanical Properties of an Ultra-High Strength Steel Hardened by Nanoscale NiAl and Cu Particles, *Acta Mater.*, 2015, **97**, p 58–67

23. Z.W. Zhang, C.T. Liu, Y.R. Wen, A. Hirata, S. Guo, G. Chen, M.W. Chen, and B.A. Chin, Influence of Aging and Thermomechanical Treatments on the Mechanical Properties of a Nanocluster-Strengthened Ferritic Steel, *Metall. Mater. Trans. A*, 2012, **43**, p 351–359

24. R.D.K. Misra, H. Nathani, J.E. Hartmann, and F. Siciliano, Microstructural Evolution in a New 770 MPa Hot Rolled Nb-Ti Micro-alloyed Steel, *Mater. Sci. Eng. A*, 2005, **394**, p 339–352

25. H. Xie, L.-X. Du, J. Hu, and R.D.K. Misra, Microstructure and Mechanical Properties of a Novel 1000 MPa Grade TMCP Low Carbon Microalloyed Steel with Combination of High Strength and Excellent Toughness, *Mater. Sci. Eng. A*, 2014, **612**, p 123–130

26. X.-L. Li, C.-S. Lei, X.-T. Deng, Z.-D. Wang, Y.-G. Yu, G.-D. Wang, and R.D.K. Misra, Precipitation Strengthening in Titanium Microalloyed High-Strength Steel Plates with New Generation-Thermomechanical Controlled Processing (NG-TMCP), *J. Alloys Compd.*, 2016, **689**, p 542–553

27. Z. Peng, L. Li, J. Gao, and X. Huo, Precipitation Strengthening of Titanium Micro-Alloyed High-Strength Steel Plates with Isothermal Treatment, *Mater. Sci. Eng. A*, 2016, **657**, p 413–421

28. A. Karmakara, S. Biswas, S. Mukherjee, D. Chakrabarti, and V. Kumar, Effect of Composition and Thermo-Mechanical Processing Schedule on the Microstructure, Precipitation and Strengthening of Nb-Microalloyed Steel, *Mater. Sci. Eng. A*, 2017, **690**, p 158–169

29. F. Fletcher, Meta-analysis of T_{NR} Measurements: determining new empirical models based on composition and strain, in *Austenite Processing Symposium (Internal Company Presentation)* (2008), pp. 1–14

30. C. Ma, L. Hou, J. Zhang, and L. Zhuang, Influence of Thickness Reduction per Pass on Strain, Microstructures and Mechanical Properties of 7050 Al Alloy Sheet Processed by Asymmetric Rolling, *Mater. Sci. Eng. A*, 2016, **650**, p 454–468

31. C. Jun, T. Shuai, L. Zhen-Yu, and W. Guo-Dong, Microstructural Characteristics with Various Cooling Paths and the Mechanism of Embrittlement and Toughening in Low-Carbon High Performance Bridge Steel, *Mater. Sci. Eng. A*, 2013, **559**, p 241–249

32. N. Tsuji, R. Ueji, Y. Minamino, and Y. Saito, A New and Simple Process to Obtain Nano-Structured Bulk Low-Carbon Steel with Superior Mechanical Property, *Scr. Mater.*, 2002, **46**(4), p 305–310

33. S. Queyreau, G. Monnet, and B. Devincre, Orowan Strengthening and Forest Hardening Superposition Examined by Dislocation Dynamics Simulations, *Acta Mater.*, 2010, **58**, p 5586–5595

34. R.D.K. Misra, Z. Jia, R. O'Malley, and S.J. Jansto, Precipitation Behavior During Thin Slab Thermomechanical Processing and Isothermal Aging of Copper-Bearing Niobium-Microalloyed High Strength Structural Steels: The Effect on Mechanical Properties, *Mater. Sci. Eng. A*, 2011, **528**, p 8772–8780

35. M.P. Phaniraj, Y.-M. Shin, J. Lee, N.H. Goo, D.-I. Kim, J.-Y. Suh, W.-S. Jung, J.-H. Shim, and I.-S. Choi, Development of High Strength Hot Rolled Low Carbon Copper-Bearing Steel Containing Nanometer Sized Carbides, *Mater. Sci. Eng. A*, 2015, **633**, p 1–8

36. R.K. Ray and J.J. Jonas, Transformation Textures in Steels, *Int. Mater. Rev.*, 1990, **35**, p 1–36

37. K. Zhu, O. Bouaziz, C. OberbilligHuang, and M. Huang, An Approach to Define the Effective Lath Size Controlling Yield Strength of Bainite, *Mater. Sci. Eng. A*, 2010, **527**(24–25), p 6614–6619

38. S. Chen, Y.G. An, and C. Lahaije, Toughness Improvement in Hot Rolled HSLA Steel Plates Through Asymmetric Rolling, *Mater. Sci. Eng. A*, 2015, **625**, p 374–379

39. B. Hutchinson, J. Hagström, O. Karlsson, D. Lindell, M. Tornberg, F. Lindberg, and M. Thuvander, Microstructures and Hardness of As-Quenched Martensites (0.1–0.5%C), *Acta Mater.*, 2011, **59**, p 5845–5858

40. Y. You, C. Shang, N. Wenjin, and S. Subramanian, Investigation on the Microstructure and Toughness of Coarse Grained Heat Affected Zone in X-100 Multi-Phase Pipeline Steel with High Nb Content, *Mater. Sci. Eng. A*, 2012, **558**, p 692–701

41. A.J. Kaijalainen, P. Suikkanen, L.P. Karjalainen, and J.J. Jonas, Effect of Austenite Pancaking on the Microstructure, Texture, and Bendability of an Ultrahigh-Strength Strip Steel, *Metal. Mater. Trans. A.*, 2014, **45**, p 1273–1283

42. B.C. De Cooman, Structure-Properties Relationship in TRIP Steels Containing Carbide-Free Bainite, *Curr. Opin. Solid State Mater. Sci.*, 2004, **8**, p 285–303

43. P. Wang, S.P. Lu, N.M. Xiao, D.Z. Li, and Y.Y. Li, Effect of Delta Ferrite on Impact Properties of Low Carbon 13Cr-4Ni Martensitic Stainless Steel, *Mater. Sci. Eng. A*, 2010, **527**, p 3210–3216

44. A.A. Gornia and P.R. Mei, Effect of Controlled-Rolling Parameters on the Ageing Response of HSLA-80 Steel, *J. Mater. Process. Technol.*, 2008, **197**, p 374–378

45. B. Mishra, K. Kumbhar, K.S. Kumar, K.S. Prasad, and M. Srinivas, Effect of Copper Addition on Microstructure and Mechanical Properties of Ultrahigh Strength NiSiCrCoMo Steel, *Mater. Sci. Eng. A*, 2016, **651**, p 177–183

46. M.D. Mulholland and D.N. Seidman, Multiple Dispersed Phases in a High-Strength Low-Carbon Steel: an Atom-Probe Tomographic and Synchrotron X-Ray Diffraction Study, *Scr. Mater.*, 2009, **60**, p 992–995

47. S. Liu, H. Tana, H. Guo, C. Shang, and R.D.K. Misra, The Determining Role of Aluminum on Copper Precipitation and Mechanical Properties in Cu-Ni-Bearing Low Alloy Steel, *Mater. Sci. Eng. A*, 2016, **676**, p 510–521

48. C.N. Hulme-Smith and H.K.D.H. Bhadeshia, Mechanical Properties of Thermally-Stable, Nanocrystalline Bainitic Steels, *Mater. Sci. Eng. A*, 2017, **700**, p 714–720